Sucrose derived microporous–mesoporous carbon for advanced lithium–sulfur batteries

Nannan Wang [a], Yong Hong [a], Terence Xiaoteng Liu [b, *], Qi Wang [a], Jiarui Huang [a, *]

[a] Key Laboratory of Functional Molecular Solids, Ministry of Education, Key Laboratory of Electrochemical Clean Energy of Anhui Higher Education Institutes, College of Chemistry and Materials Science, Anhui Normal University, Wuhu 241002, P.R. China

[b] Department of Mechanical & Construction Engineering, Faculty of Engineering and Environment, Northumbria University, Newcastle upon Tyne NE1 8ST, U.K.

Corresponding author: terence.liu@northumbria.ac.uk (X.T. Liu) and jrhuang@mail.ahnu.edu.cn (J. R. Huang).

ABSTRACT: A microporous–mesoporous carbon has been successfully prepared via carbonization of sucrose followed by heat treatment process. The obtained porous carbon possesses abundant micropores and mesopores, which can effectively increase the sulfur loading. The composite exhibited a remarkable initial capacity of 1185 mAh g^{-1} at 0.2 A g^{-1} and maintained at 488 mAh g^{-1} after 200 cycles, when employed for lithium–sulfur batteries. Moreover, the composite displayed enhanced rate capabilities of 1124, 914 and 572 mAh g^{-1} at 0.2, 0.5 and 1.0 A g^{-1}. The outstanding electrochemical capabilities and facile low–cost preparation make the new microporous–mesoporous carbon as an excellent candidate for lithium sulfur batteries.

Keywords: Li–S batteries; Cathode; Sulfur host; Porous carbon; Nanostructure

1 Introduction

Lithium–sulfur (Li–S) battery, as an advanced energy–storage device, have caught increasing attention owning to its ultrahigh theoretical capacity, low cost and minimum safety issues [1]. But there are still hurdles hinders its performance, such as inferior conductivity, dissolution of polysulfides and the shuttle effect in liquid electrolyte [2]. Meanwhile, the volume effect and slow kinetics of redox reactions in the charge/discharge process also limit cyclic stability and damage structural integrity [3]. Therefore, advanced materials with high conductivity and porous structure for cathode are the key research areas for the purpose of enhancing the cyclic capacity and rate capability.

Recently, metal oxides [4], metal sulfides [5], carbon nanotube [6], and porous carbon [7] have been developed as sulfur host materials. Among these materials, porous carbon can capture highly dispersive sulfur particulates, improve the conductivity and alleviate the volume effect [8–9]. However, common micro–structured porous carbon shows low surface areas, low porosities, and poor sulfur loading, which lead to the low sulfur utilization and rate capabilities [10]. Vast approaches have been paid to optimize the microstructures of the porous carbon in terms of solve aforementioned problems. Strategies of obtaining high porous carbon materials can be classified into the following major categories: i) Biomass materials, as a vital resource of porous carbon materials, has drawn extensive attention due to the naturally abundance and low cost [11]. E.g. activated pomelo peels [12], litchi shells [13], corncob [14] etc. derived carbon embedded with sulfur composite applied for Li–S batteries. Zhang and colleagues designed an activated carbon via carbonizing the mango stone. The as–prepared cathode possesses a tunable porous structure and delivered a capacity of 536 mAh g^{-1} over 500 cycles at 0.675 A g^{-1} [15]. ii) Chemical

reagents such as glucose [16], urea [17] and polymer composite [18] etc. can be carbonized and then served as sulfur host. For example, Yao et al. prepared a graphitic carbon nitride via thermal–pyrolysis of urea, which exhibited a capacity of 605.4 mAh g^{-1} after 500 cycles at 0.39 mA cm^{-2} [19]. iii) Template method which has been used to the synthesis of porous carbon materials. Many templates such as silica pellets [20], porous silica [21], molecular sieves [22] etc. have been developed in recent years as sulfur host. For example, a three–dimensional porous carbon was synthesized using SiO_2 nanospheres template followed by adding sulfur applied to Li–S battery, the composite achieved capacity of 760 mAh g^{-1} over 150 cycles at 0.1675 A g^{-1} [23]. iv) Metal organic frameworks (MOFs) materials derived nanostructured porous carbon [24], such as zeolitic imidazolate frameworks (ZIFs) [25] and materials of Institute Lavoisier (MIL) series [26] shows high surface area and suitable pore size after carbonation. For example, Wei et al carbonized a mixture of ZIF–67 and dicyandiamide precursors to prepare N–Doped carbon nanotubes [27], when applied for Li–S batteries, it exhibited a capacity of 3.73 mAh cm^{-2} over 100 cycles at 0.1C. However, these methods are very complex and some of the methods involves high–cost ligand reagent, which limits their scale–up production. It is urgently demanded to develop an efficient, large–scale and low–cost method to prepare porous carbon sulfur host.

Herein, a facile and scalable strategy was designed to prepare a nanostructured porous carbon (PC) with abundant micropores and mesopores. The PC was obtained using sucrose as carbon source, via a concentrated sulfuric carbonization and a subsequent heat treatment process. When applied in sulfur host, the PC/S composite demonstrates a high reversible capacity and a superior rate performance.

2 Experimental section

2.1 Preparation of porous carbon (PC)

All chemicals are purchased from Aladdin, and used as received. 15.0 g of sucrose was added into 30 ml of concentrated sulfuric acid solution (98%), then the mixtures were transferred into an oven and carbonized at 120 °C for 40 minutes. Then the resulting black product was washed with distilled water six times and dried at 80 °C for 20 h. Then, the black product was calcined in Ar at 800 °C for 3 h. After that, the obtained sample was smashed via planetary ball–milling at 400 r min^{-1} for 4 h. Finally, the PC sample was collected.

2.2 Preparation of PC/S composite

Briefly, the as–prepared PC was mixed with commercial sulfur powder along with the mass ratio of 1:3. Then, the composites were sealed in a Teflon–lined container in Ar–filled atmosphere, and heated at 160 °C for 50 h. Finally, the PC/S composite was obtained. Commercially available sulfur powder (Aladdin, S111724) is also included as cathode for comparison propose.

2.3 Li–S batteries assembly and testing (see Supplementary Information for details).

3 Results and discussion

3.1 Structural and morphological characterization

The scanning electron microscopy (SEM) images demonstrate the structure and morphology of the PC samples. The SEM results are exhibited in Figs. 1a,b, the PC before ball milling process exhibits the numerous irregular bulk structure ranging in size from one to a dozen micrometers, and the surface of the porous carbon is relatively smooth. Figs. 1c,d reveals a smooth morphology information of homogeneous particle sizes distribution with average size of 5 micrometer for the PC after ball–milling.

The high-resolution TEM (HRTEM) images (Figs. 2a,b) confirm the micro–porous nanostructure of the product. The inset image presents the selected area electron diffraction (SAED) pattern of the PC, in which two Debye–Scherrer rings were clearly observed. The rings represent the (104) and (116) planes of the hexagonal carbon (JCPDS no. 26–1076). These results demonstrate the evidence of amorphous profile of our porous carbon sample.

Fig. 3a shows the results of the BET measurements for the PC sample. The isotherm curves of PC are a combination of Type I (characteristic of microporous materials) and Type IV (typical feature of mesoporous structure) isotherms [28]. As shown in Fig. 3a (inset), PC contains pores with the sizes in the 0.355-28.0 nm, indicating the coexistence of micropores and mesopores. Together with the micropores observed in the TEM images, these measurements confirm the micro–meso porous structure of PC. The specific surface area and total pore volume of PC are approximately 480.5 $m^2 g^{-1}$ and 0.231 $cm^3 g^{-1}$, respectively. Consequently, the composite's abundant surface area and high total pore volume can accommodate high sulfur content and anchor the polysulfides in redox process [29].

X-ray diffraction (XRD) measurements were performed to investigate the crystal structures of the PC and PC/S. As for the XRD pattern of PC shown in Fig. 3b, a broad peak at ca. 26° can be observed, which attributes to the (002) peak of amorphous carbon [30]. As for the pattern of PC/S composite, the characteristic peaks are similar with the peaks of sulfur, and the intensities of diffraction peaks are weaker than these of sulfur, indicating the PC material was combined with sulfur powder in the composite, the peak of sulfur powder is consistent with the characteristic peaks of orthorhombic sulfur (JCPDS no. 08–0247) [31].

X-ray photoelectron spectroscopy (XPS) measurement for PC/S composite was performed to study the valence state of element. The XPS survey spectrum of PC/S composite is shown in Fig. S3. The C1s spectrum presented in Fig. 4a can be divided into three peaks located at approximately 284.7, 285.9 and 289.5 eV, corresponding to the C–C/C=C, C–O and O–C=O bonds, respectively [32]. In the S 2p spectrum (Fig. 4b), a weak broad peak in the range of 169.8 eV to 166.8 eV can be ascribed to the S–O bond of sulfate species arising from the oxidation of the active sulfur in air [33]. Besides, the fitted peaks located at 163.8 and 164.9 eV are associated with the S–S bond of the long–chain polysulfides [34].

Raman spectroscopy has been generally performed to elucidate the structural characteristics of carbonaceous materials. As shown in Fig. 4c, both PC and PC/S samples exhibit the peaks located at 1345 and 1585 cm^{-1}, which are ascribed to the defect structure (D band) and the graphitic carbon atom in the carbon lattice (G band) [35]. The value of I_D/I_G for PC is 0.80, confirming the formation of graphite structure in the high–temperature annealing process, which facilitates the charge transport between the electrodes [36]. The defects in PC are reported to be beneficial for the sulfur loading [37]. Furthermore, the I_D/I_G value of PC/S (0.92) is higher than that of PC, which indicates that the PC/S composite generates more lattice defects after loading sulfur. In addition, the three small peaks at 153, 226 and 330 cm^{-1} are characteristic peaks of elemental sulfur [38], demonstrating the sulfur was compounded with PC successfully. The thermogravimetric analysis (TGA) was further performed to investigate the sulfur content in the PC/S composite. As shown in Fig. 4d, the result of pure sulfur demonstrates the sulfur loss at 265–316 °C. The sulfur content in PC/S composite is ca. 62.6%. And a weight loss from 500 °C is ascribed to oxidation of PC, and the content of PC in the composite is ca. 37.4% [39].

3.2 Electrochemical properties

A coin type CR2032 half–cell having lithium metal was used as counter electrode and reference electrode, and a polypropylene film was applied as separator for electrochemical testing. The electrochemical performance characteristics of PC/S composite are shown in Fig. 5. Fig. 5a presents the CV analysis of the PC/S cathode obtained at scan rate of 0.1 mV s^{-1} in the range of 1.6–2.8 V. The peak at approximately 2.33 V is ascribed to the anode reaction of Li_2S/Li_2S_2 to S_8 [40]. The two peaks presented at 2.30 V and 2.06 V correspond to the reduction of S_8 to Li_2S_n and Li_2S/Li_2S_2 in cathodic curves, respectively [41]. Compared with the first reduction reaction process at approximately 2.30 V, the second reaction process at approximately 2.06 V involves more lithium ions. Therefore, the area of the reduction peak at 2.06 V is larger than that of the reduction peak at 2.30 V. The subsequent CV curves are almost identical, which indicates the superior reversibility of the PC/S cathode [42]. Moreover, the CV curves obtained at a scan rate of 0.1 mV s^{-1} for commercial sulfur are presented in Fig. S1. The peaks at 2.12 and 1.83 eV on the cathodic curves are associated with the reduction of S_8 to Li_2S_n and Li_2S_2/Li_2S, respectively. One peak at 2.62 eV is due to the oxidation of Li_2S_2/Li_2S to S_8. It can be demonstrated that peaks of PC/S cathode are shaper than those of commercial sulfur from CV results, suggesting that the PC/S composite possesses a slight polarization profile [43].

Fig. 5b shows the charge/discharge curves of PC/S at 0.2 A g^{-1} for different cycles. The discharge capacities are 1185, 1103, 1076, 684 and 585 mAh g^{-1} for the 1st, 2nd, 3rd, 50th and 100th cycles. However, the discharge capacities of the 1st, 2nd, 3rd, 50th and 100th cycles are 697, 693, 683, 479 and 399 mAh g^{-1} for the pure sulfur cathode in Fig. S2, which are far lower than those of PC/S composite. The platforms

of discharge at 2.28 and 2.11 V are approximately consistent with the positions of the reduction peaks. The charge platform at 2.32 V is corresponding to the oxidation peak, which is in agreement with the CV analysis. The polarization phenomenon is gradually apparent with increasing cycle times, due to the irreversible deposition of polysulfides on the cathodes [44]. However, the gap between the discharge platforms and charge plateau of PC/S cathode is even narrower than those of pure sulfur cathode, indicating the PC/S can alleviate polarization phenomenon during the cycling process [45].

Rate capabilities from 0.1 to 1.0 A g^{-1} of the PC/S and pure sulfur cathodes are shown in Fig. 5c. The specific capacities are 946, 1124, 1041, 572 mAh g^{-1} at 0.1, 0.2, 0.5 and 1.0 A g^{-1}, respectively. After returning to 0.1 A g^{-1}, the capacity recovered to 1056 mAh g^{-1}. Contrarily, the pure sulfur cathode Li–S battery exhibits capacities of 929, 768, 645 and 401 mAh g^{-1} at the corresponding current densities, and a specific capacity reached 529 mAh g^{-1} when the current was restored to 0.1 A g^{-1}. However, decreased the first discharge specific capacity, mainly because the intermediate product polysulfide is dissolved in the organic electrolyte during the cycling process, so that the shuttle effect occurs, the Coulomb efficiency is lowered, and the reversibility is deteriorated. It is observed that that the first discharge capacity of PC/S is lower than those of the subsequent cycles. This is mainly because the electrolyte is not sufficiently used in the battery assembly process and permeates slowly. As a result, a small amount of sulfur in the micropores of the cathode material cannot participate in the electrochemical reaction in the first discharge process. Fig. 5d shows the cycling performance results of the PC/S and pure sulfur cathodes obtained at 0.2 A g^{-1}. The PC/S exhibits a discharge capacity of 1185 mAh g^{-1}, and it retained a capacity of 585 mAh g^{-1} over 100 cycles, which is much higher than that of the pure sulfur

cathode. The cycling performance results of the PC/S and sulfur cathodes are presented in Fig. 5e. The first discharge capacity of PC/S is 930 mAh g^{-1}, it is much higher than sulfur electrode material (312 mAh g^{-1}) at 1.0 A g^{-1}. The PC composite still delivered discharge capacities of 464 mAh g^{-1} after 500 cycles. In contrast, sulfur cathode delivers only 99 mAh g^{-1} after 500 cycles. The cycling performance results of the PC/S and sulfur cathodes at current density of 0.1 A g^{-1} are shown in Fig. S4. Both Coulombic efficiency of PC/S and pure sulfur cathodes are ~99%. The capacity of the pure sulfur cathode is much lower than that of the PC/S cathode, indicating that the porous structured carbon can increase the sulfur loading and reduce the polysulfide shuttle effect. Therefore, the discharge specific capacity is improved [46]. The SEM images of PC/S cathode after cycling test are shown in Fig. S5. It can be seen that the sample still retains its original morphology. Moreover, the cycling performance of the PC/S is comparable to those of the mesoporous carbon microtube/S [47], tubular amorphous C@S composite [48] and C@PC/S composite etc. [49–53] that are listed in Table S1. Despite that the corresponding literatures has reported a significant progress, the satisfactory electrochemical capabilities of PC/S cathode may ascribe to the following advantageous properties. First, the presences of nanostructure can accelerate the electrons/ions diffusion and facilitate electrolyte infiltration during the cycle process, improving the rate performances of cathode. Second, the porous carbon structure can capture the polysulfide and relieve the shuttle effect via physical confinement. Finally, the abundant surface area of the composite can load a high sulfur content and anchor the polysulfides in the electrochemical process. The ohmic drop represents the potential difference after various cycles and reveals the energy barrier. It is observed from Fig. 5e that the ohmic drops of the PC/S and sulfur cathodes prior to the cycling test were determined as 0.83 and 3.67 mV, respectively.

After 500 cycles, the ohmic drops of the PC/S and sulfur cathodes increased to 1.22 and 6.24 mV, respectively, which was attributed to the gradual increase of the resistance of the electrolyte and the internal resistance of the sample during the cycling process.

At various scanning rates of PC/S cathode for the Li–S battery, CV scans are conducted in scan rate of 0.1–1.0 mV S^{-1}. As shown in Fig. 6a, several mechanisms obey the total charge stored during cycling [54], and they can be qualitatively analyzed according to:

$$i = aV^b \quad (1)$$

$$log\ i = b log\ v + log\ a \quad (2)$$

where a and b are constants, i and v are the current and the scan rate, respectively. The value of b (0.5) indicates that the charge–storage process is controlled by the diffusion, and the capacitive performance of the cathode can be obtained based on the b value (1.0) [55,56]. For the anodic and cathodic peaks in Fig. 6b, the b values were determined to be 0.565, and 0.842, respectively, indicating a capacitive–controlled behavior process. Fig. 6c shows the contribution of capacity at different scan rates. The rate of the capacitive contribution is over 50%, indicating an increased capacitive contribution [57,58]. The capacitive contribution degree reaches to 83.5% at 1.0 mV s^{-1}. The PC/S cathode exhibits a superb conductivity and the abundant specific surface area, contributing to an enhanced rate performance and improved cycling performance.

Electrochemical impedance spectroscopy (EIS) measurements for PC/S and sulfur cathodes before and after cycling are shown in Fig. 7 with the inset of a schematic of the equivalent circuit. In Fig. 7a, the Nyquist plots are constituted of a high–frequency one semicircle and a low–frequency slanted line. A semicircle is

attributed to the electron transfer impedance (R_{ct}) between the electrode and the electrolyte, the inclined line at low-frequency region is related with the Li–ion diffusion in cathode material corresponding to Warburg impedance Wo [1,59]. After cycling 500 cycles, the impedance of the PC/S and pure sulfur cathodes exhibits two obvious semicircles (Fig. 7b). The high-frequency region can be ascribed to the accumulated passivation layer on the cathode surface, which is attributed to the formation of solid products (Li_2S_2/Li_2S) in the electrode. The semicircle in the medium–frequency region is associated with charge transfer resistance at the electrode–electrolyte interface [51,60]. Moreover, the low-frequency region shows an inclined line that is assigned to the Li-ion diffusion resistance [61]. The fitting results for Nyquist spectra of PC/S and commercial sulfur cathodes are presented in Table S2. The Rct values of the PC/S and pure sulfur cathodes are 50.41 Ω and 914.7 Ω prior to cycling test, indicating the PC/S material shows good conductivity [62]. Moreover, the Rct values of the PC/S and pure sulfur cathodes after 500 cycles are 25.4 Ω and 270.0 Ω, respectively. Furthermore, the Rct of the PC/S cathode after cycling is smaller than this of the fresh cathode, which demonstrates that the conductive porous carbon accelerates the electron and Li–ion diffusion while preventing the polysulfides from dissolving during the cycling process [63,64]. Furthermore, the ultraviolet (UV) spectra and the inset picture shown Fig. S6 also confirm that PC shows a stronger adsorption effect for polysulfide [11,46]. Consequently, the PC/S cathode exhibits superior electrochemical performance.

4 Conclusions

Herein, the PC/S with abundant micropores and mesopores has been successfully prepared via carbonization followed by heat treatment process. the PC/S composite with 62.0 wt% sulfur exhibits a high discharge capacity of 1185 mAh g^{-1} at 0.2 A g^{-1}

and retained at 585 mAh g^{-1} over 100 cycles, when applied for Li–S batteries. Moreover, it exhibits a capacity of 464 mAh g^{-1} at 1.0 A g^{-1} after 500 cycles. Within the composite, the nanostructured PC can provide vast number of active reaction site with large contact area to ensure an abundant sulfur loading, effectively inhibit the dissolution and the shuttle effect of polysulfides, therefore enhanced the structural stability. Our results are promising in developing high sulfur loading cathode materials for long cycle–life Li–S batteries and demonstrates a promising direction for the facile preparation of high–performance sulfur host carbon materials.

Acknowledgements

Natural Science Research Project for Universities in Anhui Province (KJ2018B14), Science and Technology Major Project of Anhui Province (18030901093), Key Research and Development Program of Wuhu (2019YF07).

Appendix A Supplementary data

Supplementary data to this article can be found online at

References

[1] X. Yi, F.Q. Zhang, B. Zhang, W.J. Yu, Q.Y. Dai, S.Y. Hu, W.J. He, H. Tong, J.C. Zheng, J.Q. Liao, (010) facets dominated $LiFePO_4$ nano–flakes confined in 3D porous graphene network as a high–performance Li–ion battery cathode, Ceram. Int. 44 (2018) 18181–18188.

[2] Z.W. Wang, S.P. Wang, Synergistic suppression of the shuttle effect and absorption of electrolytes using a functional rich amine porous organic polymer/acetylene black–polypropylene separator in Li–S batteries, Electrochim. Acta 306 (2019) 229–237.

[3] W.J. Lin, G.Q. He, Y.H. Huang, X.Y. Chen, 3D hybrid of Co_9S_8 and N–doped carbon hollow spheres as effective hosts for Li–S batteries, Nanotechnology 31 (2020) 035404.

[4] Z.H. Sun, Y.P. Guo, B. Li, T.Z. Tan, Y. Zhao, ZnO/carbon nanotube/reduced graphene oxide composite film as an effective interlayer for lithium/sulfur batteries, Solid State Sci. 95 (2019) 105924.

[5] S. Liu, Z.F. Zhou, D.C. Liu, MoS_2 coated separator as an efficient barrier for inhibiting shuttle effect of polysulfide, Ceram. Int. 45 (2019) 14415–14419.

[6] J.Y. Wang, W.J Wang, Y.G. Zhang, Y. Wang, Y. Zhao, Synthesis of CoO nanocrystals decorated porous carbon nanotube microspheres as sulfur host for high performance Li/S batteries, Nanotechnology 31 (2020) 025403.

[7] D.D. Cheng, Y.L. Zhao, T. An, X. Wang, H. Zhou, T.X. Fan, 3D interconnected crumpled porous carbon sheets modified with high–level nitrogen doping for high performance lithium sulfur batteries, Carbon 154 (2019) 58–66.

[8] N.N. Guo, S. Zhang, L.X. Wang, D.Z. Jia, Application of plant–based porous carbon for supercapacitors, Acta Phys–Chim. Sin. 36 (2020) 1903055.

[9] X.X. He, Y.P. Cheng, B. Hu, Z.Y. Wang, C.H. Wang, M.H. Yi, L. Wang, Effects of coal pore structure on methane–coal sorption hysteresis: An experimental investigation based on fractal analysis and hysteresis evaluation, Fuel 269 (2020) 117438.

[10] Y.L. Yang, Y. Yu, G.Z. Ma, J.M. Nan, H.Y. Chen, Z.Y. Zhang, W.Y. Lin, High–performance lithium−sulfur batteries fabricated from a three dimensional porous reduced graphene oxide/La_2O_3 microboards/sulfur aerogel, Ceram. Int. 45 (2019) 9017–9024.

[11] Z.F. Wang, X.M. Zhang, X.L. Liu, Y.G. Zhang, W.M. Zhao, Y.Y. Li, C.L. Qin, Z. Bakenov, High specific surface area bimodal porous carbon derived from biomass reed flowers for high performance lithium–sulfur batteries, J. Colloid Interf. Sci. 569 (2020) 22–33.

[12] H.J. Wu, D. Xiao, J.Y. Lu, C. Jiao, S.S. Li, Y.L. Lei, D.H. Liu, J.C. Wang, Z.Q. Zhang, Y.T. Liu, G.H. Shen, S.S. Li, Effect of high–pressure homogenization on microstructure and properties of pomelo peel flour film–forming dispersions and their resultant films, Food Hydrocoll. 102 (2020) 1056.

[13] N. Zhao, P.X. Zhang, D.W. Luo, W.D. Xiao, L.B. Deng, F. Qiao, Direct production of porous carbon nanosheets/particle composites from wasted litchi shell for supercapacitors, J. Alloys Compd. 788 (2019) 677–684.

[14] Z.G. Xu, Z. Geng, G.H. Yi, C. Chen, M.Z. Xue, B. Li, C.M. Zhang, Corncob–derived porous carbon as an interlayer coating to improve the performance of lithium sulfur battery, Int. J. Electrochem. Sci. 12 (2017) 4515–4527.

[15] S.T. Zhang, M.B. Zheng, Z.X. Lin, R. Zang, Q.L. Huang, H.G. Xue, J.M. Cao, H. Pang, Mango stone–derived activated carbon with high sulfur loading as a cathode material for lithium–sulfur batteries, RSC Adv. 6 (2016) 39918–39925.

[16] X.G. Li, B.Y. Guan, S.Y. Gao, X.W. Lou, A general dual–templating approach to biomass–derived hierarchically porous heteroatom–doped carbon materials for enhanced electrocatalytic oxygen reduction, Energ. Environ. Sci. 12 (2019) 648–655.

[17] Y.G. Liu, W.K. Wang, A.B. Wang, Z.Q. Jin, H.L. Zhao, Y.S. Yang, N–doped carbyne polysulfide as cathode material for lithium/sulfur batteries, Electrochim. Acta 232 (2017) 142–149.

[18] A. Hoefling, Y.J. Lee, P. Theato, Sulfur–based polymer composites from vegetable oils and elemental sulfur: A sustainable active material for Li–S batteries, Macromol. Chem. Phys. 218 (2017) 1600303.

[19] S.S. Yao, S.K. Xue, S.H. Peng, M.X. Jing, X.Y. Qian, X.Q. Shen, T.B. Li, Y.H. Wang, Synthesis of graphitic carbon nitride at different thermal–pyrolysis temperature of urea and it application in lithium–sulfur batteries, J. Mater. Sci–Mater. El. 29 (2018) 17921–17930.

[20] B.M. Covaciu, E. Richter, M. Walczak, J.–C. Tan, J.M. del Valle, A method for fabricating stainless steel pellets with open–cell porosity by alkaline leaching of silica template, Adv. Eng. Mater. 18 (2016) 1616–1625.

[21] M. Prokopowicz, A. Szewczyk, A. Skwira, R. Sądej, G. Walker, Biphasic composite of calcium phosphate–based mesoporous silica as a novel bone drug delivery system, Drug Deliv. Transl. Re. 10 (2020) 455–470.

[22] M.C. Duke, J.C. Diniz da Costa, G.Q. Lu, M. Petch, P. Gray, Carbonised template molecular sieve silica membranes in fuel processing systems: permeation, hydrostability and regeneration, J. Membrane Sci. 241 (2004) 325–333.

[23] H.Y. Gu, R. Zhang, P. Wang, S.M. Xie, C.M. Niu, H.K. Wang, Construction of three–dimensional ordered porous carbon bulk networks for high performance lithium–sulfur batteries, J. Colloid Interf. Sci. 533 (2019) 445–451.

[24] E. Gulcay, I. Erucar, Molecular simulations of COFs, IRMOFs and ZIFs for adsorption–based separation of carbon tetrachloride from air, J. Mol. Graph. Model. 86 (2019) 84–94.

[25] Z.Q. Wang, L.M. Yang, S.L. Liu, H.J. Yu, X.N. Li, Y. Xu, L. Wang, H.J. Wang, ZIF–derived porous carbon composites coated on $NiCo_2S_4$ nanotubes array toward efficient water splitting, Nanotechnology 31 (2020) 195402.

[26] Z.Q. Gong, S.L. Niu, Y.J. Zhang, C.M. Lu, Facile synthesis of porous α–Fe_2O_3 nanostructures from MIL–100(Fe) via sacrificial templating method, as efficient catalysts for NH_3–SCR reaction, Mater. Res. Bull. 123 (2020) 110693.

[27] T. Long, F.C. Meng, B. Xu, Y.X. Zhao, W.L. Liu, X.F. Wei, L.X. Zheng, J.H. Liu, Nitrogen-doped carbon nanotubes intertwined with porous carbon with enhanced cathode performance in lithium–sulfur batteries, Sustain. Energ. Fuels 4 (2020) 3926-3933.

[28] D.P. Li, X.H. Ren, Q. Ai, Q. Sun, L. Zhu, Y. Liu, Z. Liang, R.Q. Peng, P.C. Si, J. Lou, J.K. Feng, L.J. Ci, Facile fabrication of nitrogen–doped porous carbon as superior anode material for potassium–ion batteries, Adv. Energy Mater. 8 (2018) 1802386.

[29] T. Chen, Z.W. Zhang, B.R. Cheng, R.P. Chen, Y. Hu, L.B. Ma, G.Y. Zhu, J. Liu, Z. Jin, Self–templated formation of interlaced carbon nanotubes threaded hollow Co_3S_4 nanoboxes for high–rate and heat–resistant lithium−sulfur batteries, J. Am. Chem. Soc. 139 (2017) 12710–12715.

[30] Z.L. Chen, S.P. Cheng, Y.X. Chen, X.H. Xia, H.B. Liu, Pomegranate–like S@N–doped graphitized carbon spheres as high–performance cathode for lithium–sulfur battery, Mater. Lett. 263 (2020) 127283.

[31] R. Elazari, G. Salitra, A. Garsuch, A. Panchenko, D. Aurbach, Sulfur–impregnated activated carbon fiber cloth as a binder–free cathode for rechargeable Li–S batteries, Adv. Mater. 23 (2011) 5641–5644.

[32] G.D. Park, Y.C. Kang, Aerosol–assisted synthesis of porous and hollow carbon–carbon nanotube composite microspheres as sulfur host materials for high–performance Li–S batteries, Appl. Surf. Sci. 495 (2019) 143637.

[33] J.Q. Huang, Z.L. Xu, S. Abouali, M.A. Garakani, J.K. Kim, Porous graphene oxide/carbon nanotube hybrid films as interlayer for lithium–sulfur batteries, Carbon 12 (2016) 081.

[34] X.J. Chen, G.H. Du, M. Zhang, A. Kalam, Q.M. Su, S.K. Ding, B.S. Xu, Nitrogen-doped hierarchical porous carbon derived from low-cost biomass pomegranate residues for high performance lithium-sulfur batteries, J. Electroanal. Chem. 848 (2019) 113316.

[35] Q.N. Zhao, K.Q. Zhao, G.P. Ji, X.L. Guo, M. Han, J. Wen, Z.L. Ren, S.C. Zhao, Z. Gao, R.H. Wang, M. Li, K. Sun, N. Hu, C.H. Xu, High sulfur loading, rGO–linked and polymer binder–free cathodes based on rGO wrapped N, P–codoped mesoporous carbon as sulfur host for Li–S batteries, Chem. Eng. J. 361 (2019) 1043–1052.

[36] C. Li, X. L. Sui, Z.B. Wang, Q. Wang, D.M. Gu, One–step synthesis of 3D N–doped graphene supported metal oxide for high performance Li–S battery, Ceram. Int. 44 (2018) 13419–13425.

[37] M.W. Xiang, L. Yang, Y.F. Zheng, J. Huang, P. Jing, H. Wu, Y. Zhang, H. Liu, A freestanding and flexible nitrogen–doped carbon foam/sulfur cathode composited with reduced graphene oxide for high sulfur loading lithium–sulfur batteries, J. Mater. Chem. A, 5 (2017) 18020–18028.

[38] L.L. Gao, Y.X. Cao, J. Wang, H.B. Ren, J.H. Wang, J.R. Huang, Construction of polypyrrole coated hollow cobalt manganate nanocages as an effective sulfur host for lithium-sulfur batteries, Ceram. Int. 46 (2020) 18224–18233.

[39] F. Wu, S.Y. Zhao, L. Chen, Y. Lu, Y.F. Su, J. Li, L.Y. Bao, J.Y. Yao, Y.W.

Zhou, R.J. Chen, Electron bridging structure glued yolk–shell hierarchical porous carbon/sulfur composite for high performance Li–S batteries, Electrochim. Acta 292 (2018) 199–207.

[40] D.W. Wang, G.M. Zhou, F. Li, K.H. Wu, G.Q. Lu, H.M. Cheng, I.R. Gentle, A microporous–mesoporous carbon with graphitic structure for a high–rate stable sulfur cathode in carbonate solvent–based Li–S batteries, Phys. Chem. Chem. Phys. 14 (2012) 8703–8710.

[41] D. Li, F. Han, S. Wang, F. Cheng, Q. Sun, W.C. Li, High sulfur loading cathodes fabricated using peapodlike, large pore volume mesoporous carbon for lithium−sulfur battery, ACS Appl. Mater. Inter. 5 (2013) 2208–2213.

[42] H.L. Wang, Y. Yang, Y.Y. Liang, J. Tucker Robinson, Y.G. Li, A. Jackson, Y. Cui, Graphene–wrapped sulfur particles as a rechargeable lithium–sulfur battery cathode material with high capacity and cycling stability, Nano Lett. 11 (2011) 2644–2647.

[43] P. Zeng, L.W. Huang, X.L. Zhang, R.X. Zhang, L. Wu, Y.G. Chen, Long–life and high–areal–capacity lithium–sulfur batteries realized by a honeycomb–like N, P dual–doped carbon modified separator, Chem. Eng. J. 349 (2018) 327–337.

[44] P. Zhou, T.L. Han, C.P. Gu, J.J. Li, Z.H. Shen, H.G. Zhang, J.J. Niu, J.H. Liu, J.Y. Liu, A novel wheel–confined composite as cathode in Li–S batteries with high capacity retention, J. Alloys Compd. 776 (2019) 504–510.

[45] L.L. Gao, C.P. Gu, H.B. Ren, X.J. Song, J.R. Huang, Synthesis of tin(IV) oxide@reduced graphene oxide nanocomposites with superior electrochemical behaviors for lithium–ions batteries, Electrochim. Acta 290 (2018) 72–81.

[46] P.Y. Li, J.N. Deng, J. Li, L.G. Wang, J.Q. Guo, Hollow graphene spheres coated separator as an efficient trap for soluble polysulfides in Li–S battery, Ceram. Int. 45 (2019) 13219–13224.

[47] Y.G. Zhang, Y. Zhao, A. Konarov, Z. Li, P. Chen, Effect of mesoporous carbon microtube prepared by carbonizing the poplar catkin on sulfur cathode performance in Li/S batteries, J. Alloys Compd. 619 (2015) 298–302.

[48] S.S. Li, B. Jin, H. Li, C.W. Dong, B. Zhang, J.H. Xu, Q. Jiang, Synergistic effect of tubular amorphous carbon and polypyrrole on polysulfides in Li-S batteries, J. Electroanal. Chem. 806 (2017) 41–49.

[49] L. Zhang, R.A. Senthil, J.Q. Pan, A. Khan, X. Jin, Y.Z. Sun, A novel carbon nanotubes@porous carbon/sulfur composite as efficient electrode material for high–performance lithium–sulfur battery, Ionics 25 (2019) 4761–4773.

[50] H.L. Wu, L. Xia, J. Ren, Q.J. Zheng, F.Y. Xie, W.J. Jie, C.G. Xu, D.M. Lin, A multidimensional and nitrogen–doped graphene/hierarchical porous carbon as a sulfur scaffold for high performance lithium sulfur batteries, Electrochim. Acta 278 (2018) 83–92.

[51] Y.L. Yan, M.M. Shi, Y.M. Zou, Y.Q. Wei, L.P. Chen, C.J. Fan, R. Yang, Y.H. Xu, Tunable hierarchical porous carbon aerogel/graphene composites cathode matrix for Li–S batteries, J. Alloys Compd. 791 (2019) 952–961.

[52] W.M. Kang, L.L. Fan, N.P. Deng, H.J. Zhao, Q.X. Li, N. Minooc, J. Yan, B.W. Cheng, Sulfur–embedded porous carbon nanofiber composites for high stability lithium–sulfur batteries, Chem. Eng. J. 333 (2018) 185–190.

[53] F.H. Zhao, D. Li, B. Cao, M. Liu, K. Chen, Y. Chen, Hierarchical carbon microstructures prepared from oil-palm-shell tracheids for Li-S batteries, New J. Chem. 41 (2017) 4110–4115.

[54] D.L. Chao, P. Liang, Z. Chen, L.Y. Bai, H. Shen, X.X. Liu, X.H. Xia, Y.L. Zhao, S.V. Savilov, J.Y. Lin, Pseudocapacitive Na–ion storage boosts high rate and areal capacity of self–branched 2D layered metal chalcogenide nanoarrays, ACS Nano 10 (2016) 10211–10219.

[55] Y. Wu, W. Zhang, T.L. Han, Z.H. Shen, D. Cheng, H.K. Zhang, J.J. Li, H.G. Zhang, J.Y. Liu, A novel ternary sulfur/carbon@tin dioxide composite with polysulfides adsorptive shell and conductive core as high–performance lithium–sulfur battery cathodes, Appl. Surf. Sci. 489 (2019) 462–469.

[56] H. Li, B. Zhang, X. Ou, L.B. Tang, C.H. Wang, L. Cao, C.L. Peng, J.F. Zhang, In–situ fabrication of hetero structured SnO_x@C/rGO composite with durable cycling life for improved lithium storage, Ceram. Int. 45 (2019) 18743–18750.

[57] Z.P. Ma, F.Y. Jing, Y.Q. Fan, J.J. Li, Y. Zhao, G.J. Shao, High electrical conductivity of 3D mesporous carbon nanocage as an efficient polysulfide buffer layer for high sulfur utilization in lithium sulfur batteries, J. Alloys Compd. 789 (2019) 71–79.

[58] J.B. Li, D. Yan, X.J. Zhang, S.J. Hou, T. Lu, Y.F. Yao, L.K. Pan, ZnS nanoparticles decorated on nitrogen–doped porous carbon polyhedra: a promising anode material for lithium–ion and sodium–ion batteries, J. Mater. Chem. A 5 (2017) 20428–20438.

[59] B. Ni, Y.Q. Li, T.Q. Chen, T. Lu, L.K. Pan, Covalent organic frameworks converted N, B co–doped carbon spheres with excellent lithium ion storage performance at high current density, J. Colloid Interf. Sci. 542 (2019) 213–221.

[60] G.F. Chen, J.H. Li, N. Liu, Y. Zhao, J.G. Tao, G. Kalimuldina, Z. Bakenov, Y.G. Zhang, Synthesis of nitrogen–doped oxygen–deficient TiO_{2-x}/reduced graphene

oxide/sulfur microspheres via spray drying process for lithium–sulfur batteries, Electrochim. Acta 326 (2019) 134968.

[61] H.Y. Yan, X.X. Xue, Y.Q. Fu, X.M. Wu, J.W. Dong, Three–dimensional carbon nanotubes–encapsulated Li_2FeSiO_4 microspheres as advanced positive materials for lithium energy storage, Ceram. Int. 46 (2020) 9729–9733.

[62] S.B. Jin, X.H. Sun, S. Cai, J.Z. Guo, A.R. Fan, N. Zhang, H. Wu, C.M. Zheng, SnS_2 quantum dots uniformly anchored on dispersed S–doped graphene as high–rate anodes for sodium–ion batteries, Ceram. Int. 46 (2020) 14416–14424.

[63] J.J. Zhao, H.B. Ren, C.P. Gu, W.M. Guan, X.J. Song, J.R. Huang, Synthesis of hierarchical molybdenum disulfide microplates consisting of numerous crosslinked nanosheets for lithium–ion batteries, J. Alloys Compd. 781 (2019) 174–185.

[64] Z.X. Wang, C.X. Xu, L. Chen, J. Si, W.R. Li, S.S. Huang, Y. Jiang, Z.W. Chen, B. Zhao, In–situ lithiation synthesis of nano–sized lithium sulfide/graphene aerogel with covalent bond interaction for inhibiting the polysulfides shuttle of Li–S batteries, Electrochim. Acta 312 (2019) 282–290.

Figure captions

Fig. 1 SEM images of PC (a, b) before and (c, d) after ball–milling.

Fig. 2 (a) TEM and (b) HRTEM images of PC sample. Inset is SAED pattern of PC sample.

Fig. 3 (a) Nitrogen adsorption/desorption isotherms of PC sample, the inset shows the pore size distribution of PC sample. (b) XRD patterns of PC, PC/S and commercial sulfur powder.

Fig. 4 XPS spectra of (a) C 1s and (b) S 2p. (c) Raman spectra and (d) TGA curves of PC/S and commercial sulfur powder.

Fig. 5 (a) CV curves of PC/S composites in potential range of 1.6-2.8 V at a scan rate of 0.1 mV s^{-1}. (b) Charge/discharge profiles of PC/S composites at 0.2 A g^{-1}. (c) Rate performances of PC/S and sulfur powder cathodes. Cycling performances of PC/S and sulfur powder cathodes at current densities of (d) 0.2 A g^{-1} over 200 cycles and (e) 1.0 A g^{-1} over 500 cycles.

Fig. 6 (a) CV curves of PC/S for Li–S batteries at different scan rates ranging from 0.1 to 1 mV S^{-1}. (b) Plots of log *i* versus log *v*. (c) Percentages of capacitive contribution at different scan rates for PC/S cathode.

Fig. 7 Nyquist plots of PC/S and sulfur cathodes (a) before cycling test and (b) after 500 cycles. Insets are the corresponding simulation circuit models.

Figures

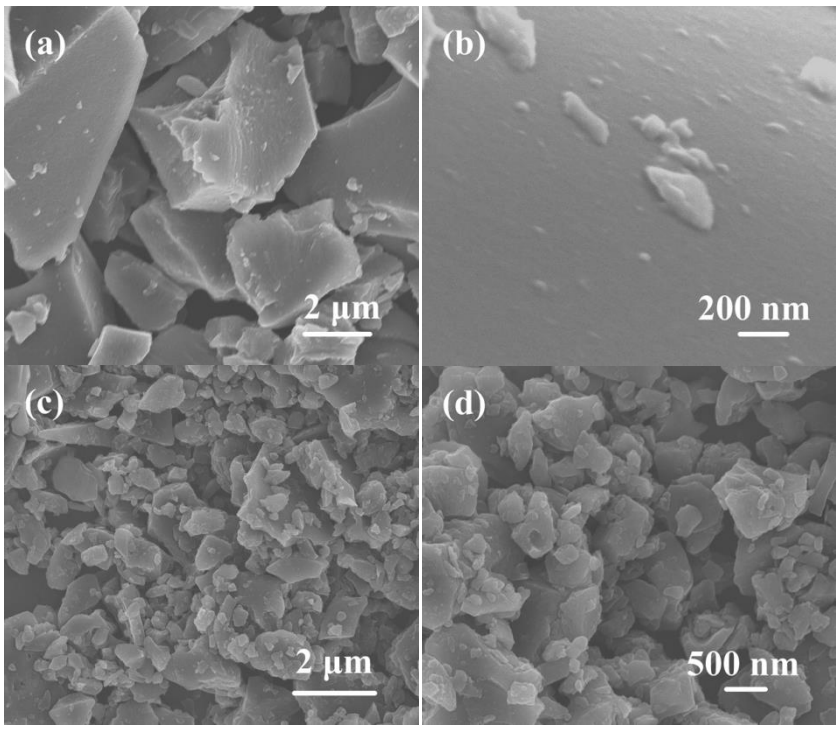

Fig. 1 SEM images of PC (a, b) before and (c, d) after ball–milling.

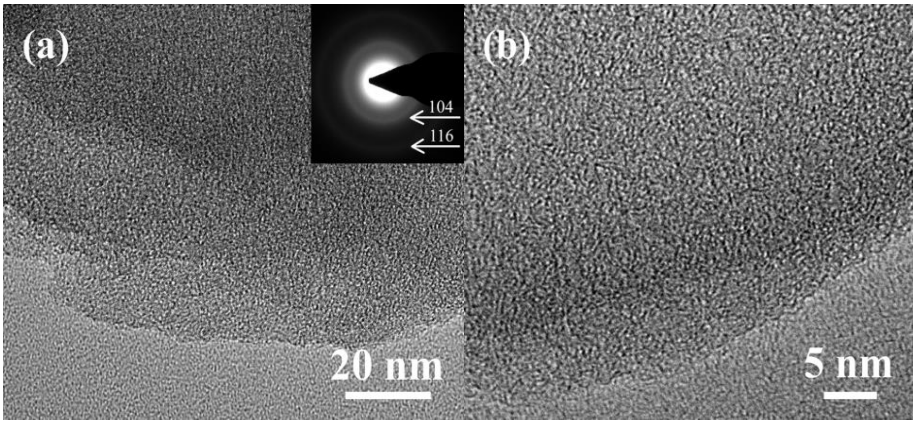

Fig. 2 (a) TEM and (b) HRTEM images of PC sample. Inset is SAED pattern of PC sample.

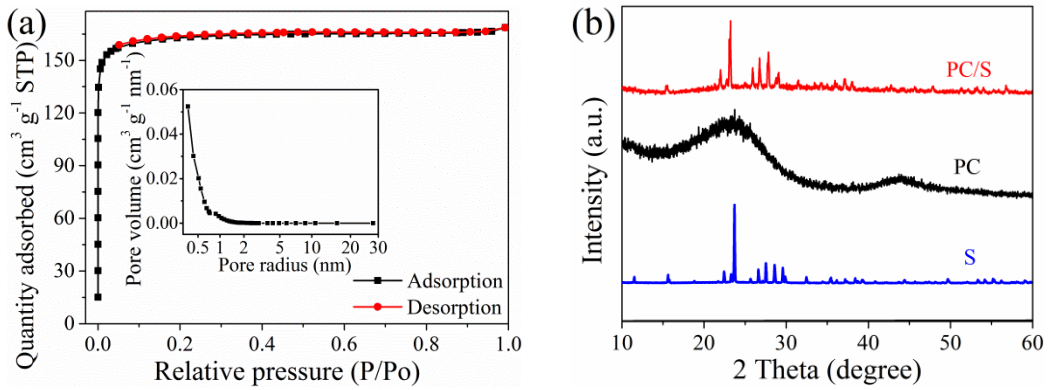

Fig. 3 (a) Nitrogen adsorption/desorption isotherms of PC sample, the inset shows the pore size distribution of PC sample. (b) XRD patterns of PC, PC/S and commercial sulfur powder.

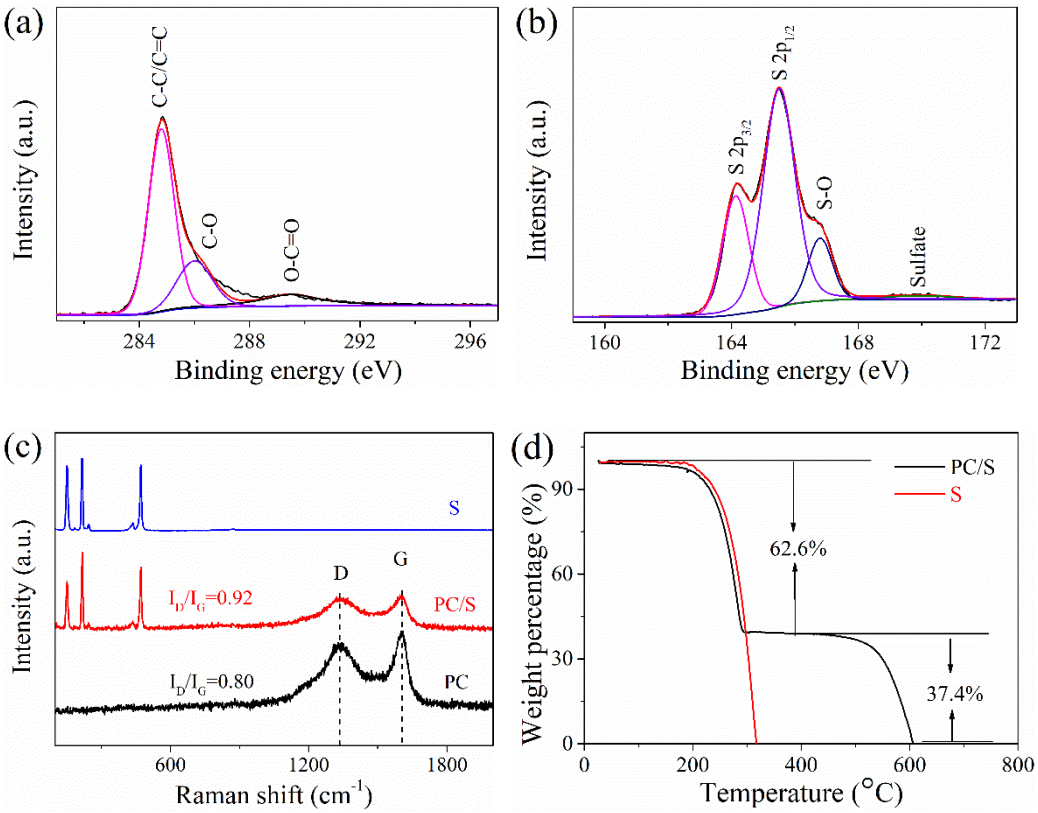

Fig. 4 XPS spectra of (a) C 1s and (b) S 2p. (c) Raman spectra and (d) TGA curves of PC/S and commercial sulfur powder.

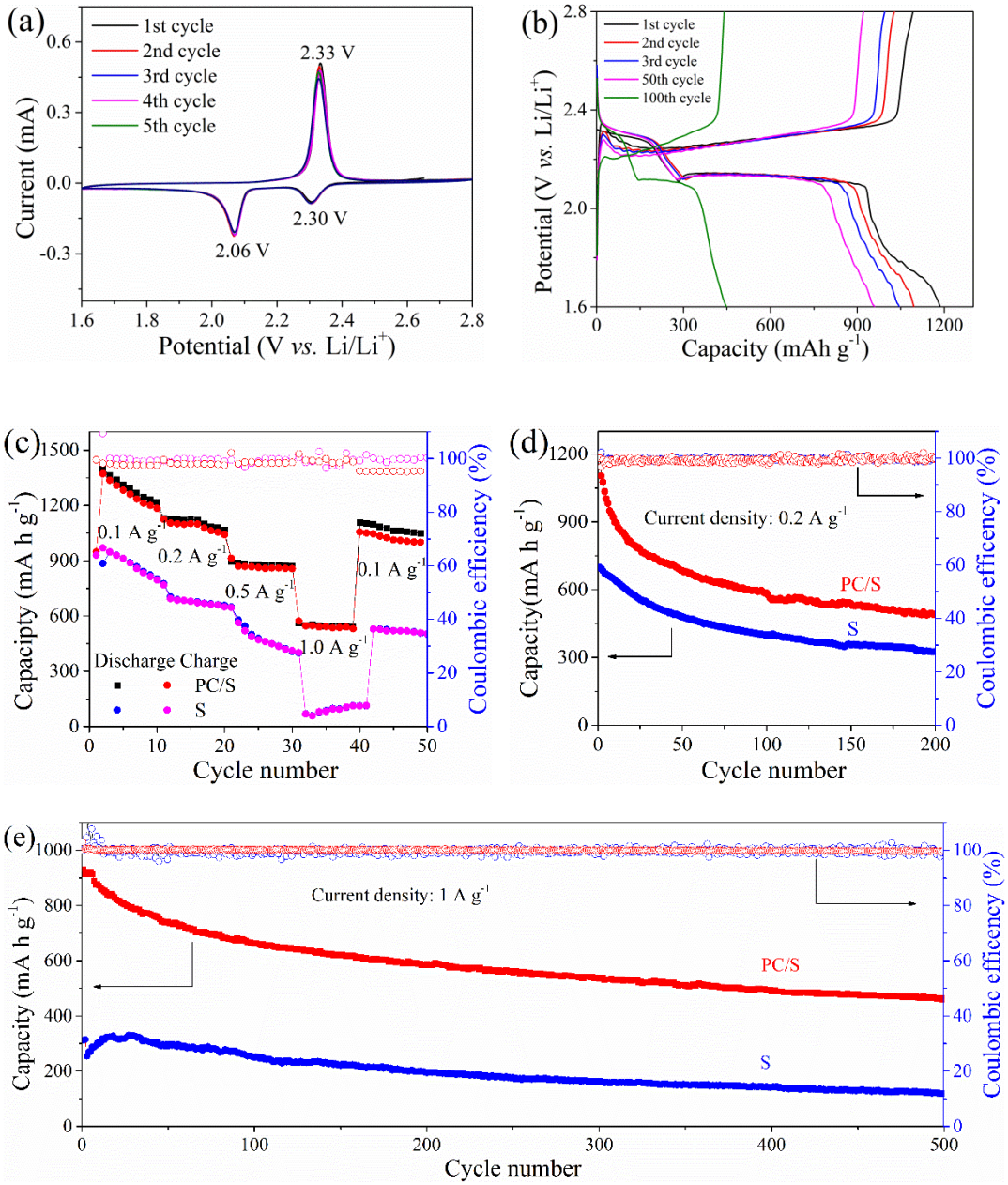

Fig. 5 (a) CV curves of PC/S composites in potential range of 1.6-2.8 V at a scan rate of 0.1 mV s^{-1}. (b) Charge/discharge profiles of PC/S composites at 0.2 A g^{-1}. (c) Rate performances of PC/S and sulfur powder cathodes. Cycling performances of PC/S and sulfur powder cathodes at current densities of (d) 0.2 A g^{-1} over 200 cycles and (e) 1.0 A g^{-1} over 500 cycles.

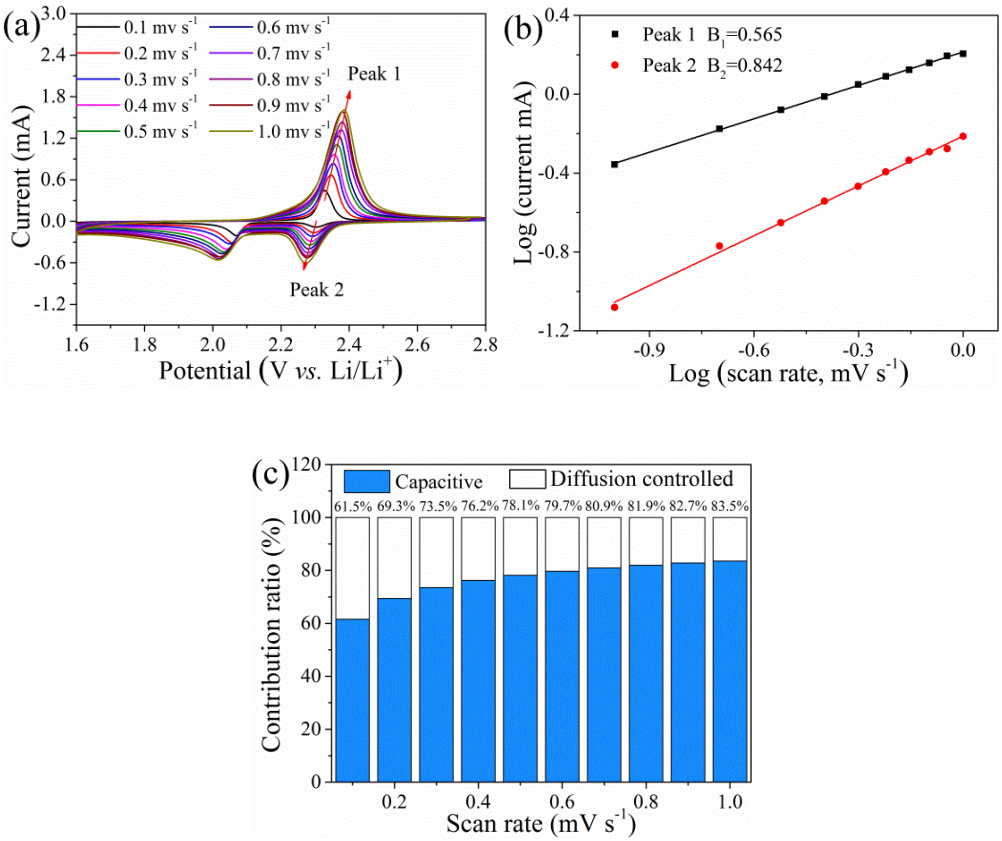

Fig. 6 (a) CV curves of PC/S for Li–S batteries at different scan rates ranging from 0.1 to 1 mV S^{-1}. (b) Plots of log *i* versus log *v*. (c) Percentages of capacitive contribution at different scan rates for PC/S cathode.

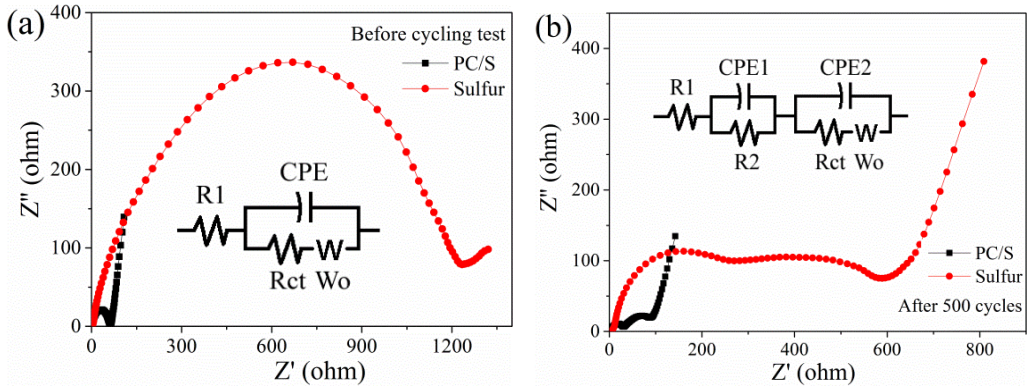

Fig. 7 Nyquist plots of PC/S and sulfur cathodes (a) before cycling test and (b) after 500 cycles. Insets are the corresponding simulation circuit models.